Inorganic Chemistry

Article

pubs.acs.org/IC

X-ray Absorption and Emission Spectroscopies of X-Bridged Diiron Phthalocyanine Complexes $(FePc)_2X$ (X = C, N, O) Combined with DFT Study of $(FePc)_2X$ and Their High-Valent Diiron Oxo Complexes

Cedric Colomban,[†] Evgenij V. Kudrik,[†,‡] Valerie Briois,[§] Janine C. Shwarbrick,[⊥] Alexander B. Sorokin,*[,†] and Pavel Afanasiev*[,†]

[†]Institut de Recherches sur la Catalyse et l'Environnement de Lyon, IRCELYON, UMR 5256, CNRS−Université Lyon 1, 2, Avenue Albert Einstein, 69626 Villeurbanne, France

[‡]State University of Chemistry and Technology, Engels Street 7, 153000 Ivanovo, Russia

[§]Synchrotron SOLEIL, L'Orme des Merisiers, Saint Aubin BP48, Gif sur Yvette, FR 91192, France

[⊥]European Synchrotron Radiation Facility (ESRF), 38043 Grenoble 9, France

Supporting Information

ABSTRACT: μ-Nitrido diiron phthalocyanine $[PcFe^{+3.5}NFe^{+3.5}Pc]^0$ is an efficient catalyst, able to catalyze the oxidation of methane under near-ambient conditions. In this work, we compared the properties of structurally similar μ-carbido (**1**), μ-nitrido (**2**), and μ-oxo (**3**) dimers of iron phthalocyanine. The goal was to discern the structural and electronic differences between these complexes and to propose a rationale for the exceptional activity of **2**. Extended X-ray fine-structure spectroscopy, high-resolution X-ray emission spectroscopy, and resonant inelastic X-ray scattering were applied to study the geometry and electronic structure of iron species in the series **1**−**3**. The data provided by core hole spectroscopies were compared to the results of DFT calculations and found to coherently describe the structural and electronic properties of **1**−**3** as having equivalent iron centers with formal iron oxidation degrees of 3, 3.5, and 4 for the μ-oxo, μ-nitrido, and μ-carbido dimers, respectively. However, the bond length to the bringing atom changed in an unexpected sequence Fe−O > Fe−N < Fe−C, indicating redox non-innocence of the brigding μ-carbido ligand in **1**. According to the X-ray emission spectroscopy, the μ-nitrido dimer **2** is a low-spin compound, with the highest covalency in the series **1**−**3**. The DFT-calculated geometry and electronic structures as well as core hole spectra of hypothetical high-valent oxo complexes of **1**−**3** were compared, in order to explain the particular catalytic activity of **2** and to estimate the prospects of spectroscopic observation of such species. It appears that the terminal Fe═O bond is the longest in the oxo complex of **2**, due to the strong trans-effect of the nitrido ligand. The corresponding LUMO of the μ-nitrido diiron oxo complex has the lowest energy among the three oxo complexes. Therefore, the oxo complex of **2** is expected to have the highest oxidative power.

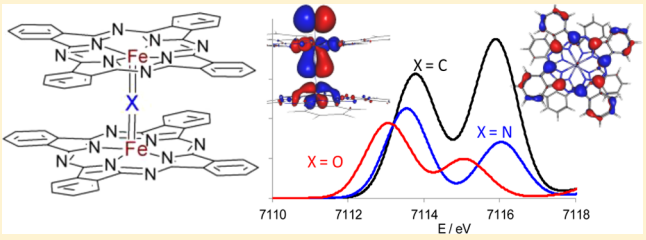

1. INTRODUCTION

Low-temperature conversion of hydrocarbons and particularly of methane is a long-standing scientific and technological challenge.[1,2] Since the discovery of the powerful oxidation properties of cytochrome P450 accociated with its iron porphyrin acive site, the functionalization of inert C−H bonds by iron complexes has been a key research topic. Much of the effort in developing synthetic catalysts able to activate C−H bonds has been inspired by the natural monooxygenase catalysts.[3] Significant progress has been made in the synthetic modeling of iron(IV)−oxo species both in biochemical and synthetic oxidation processes.[4]

Inspired by biochemical precedents we have recently proposed to use binuclear iron complexes with macrocyclic phthalocyanine[5] and porphyrin[6] ligands as catalysts for oxidation of strong C−H bonds. The N-bridged diiron porphyrin and phthalocyanine complexes have been described in the literature,[7,8] but their catalytic properties remained unexplored for a long time. We have recently demonstrated that N-bridged diiron tetra(*tert*-butyl)phthalocyanine complex containing the $Fe^{+3.5}$−N−$Fe^{+3.5}$ structural unit activated H_2O_2, leading to a very strong oxidizing species that oxidized methane in water at 25−60 °C.[5,9] The same system catalyzes oxidation of propane and ethylene[10] as well as oxidation of aromatics[11] and oxidative defluorination of perfluoroaromatics.[12] Therefore, such binuclear complexes represent a novel and promising scaffold in the oxidation catalysis. Available spectroscopic and reactivity data indicate the retention of the Fe−N−Fe binuclear structure during the catalytic cycle and the possible

Received: June 19, 2014
Published: October 22, 2014

   dx.doi.org/10.1021/ic501463q | *Inorg. Chem.* 2014, 53, 11517−11530

involvement of high-valent diiron oxo complexes as oxidizing species.[5,11,13] Notably, a mononuclear Fe(IV) oxo complex supported by a phthalocyanine ligand[14] showed a significantly lower catalytic activity.

The strong oxidizing properties have also been established for the oxo complex on the μ-nitrido diiron tetraphenylporphyrin platform, (TPP)Fe^{IV}(μ-N)Fe^{IV}=O($TPP^{+\bullet}$). The formation of the first high-valent diiron oxo complex supported by macrocyclic ligands was evidenced.[6] (TPP)Fe^{IV}(μ-N)Fe^{IV}=O($TPP^{+\bullet}$) was significantly more active than corresponding mononuclear oxo complex Fe^{IV}=O($TPP^{+\bullet}$) in the oxidation of several alkanes. Moreover, only (TPP)Fe^{IV}(μ-N)Fe^{IV}=O($TPP^{+\bullet}$) was able to react with methane. Thus, the diiron structure is essential for the high catalytic activity.

What is the reason for the high activity of μ-nitrido diiron species? The dimeric structure as such seems unlikely to be the sole cause of the unusual reactivity, as phthalocyanines are known to form various dimer and oligomer structures showing no exceptional catalytic properties.[15,16] Recently, Silaghi-Dumitrescu et al., by comparing the electronic structures of models of the μ-nitrido and μ-oxo bridged complexes, suggested that a key difference resides in the redox non-innocence of the μ-nitrido bridge.[17] However, this question requires further in-depth study as concerns both experimental evidence of the differences in the electronic structure and advanced computational models representing the initial diiron phthalocyanines and their putative oxo intermediates. Beside μ-oxo and μ-nitrido dimers, similar μ-carbido diiron species have been prepared and characterized.[18,19] The electronic structure of μ-carbido dimers has been first considered at the extended Huekel level of theory by Tatsumi et al.[20] Their comparison to the μ-nitrido and μ-oxo counterparts seems highly relevant in the context of the problem. Indeed, μ-carbido complex formally contains an Fe(IV)Fe(IV) unit and can be considered as a potential scaffold for highly oxidizing oxo species.

The mechanistic features of the formation of a powerful active species are far from being fully understood. During generation of the diiron active species, the iron atoms of the complex change the oxidation and spin states to form transient, elusive species. Direct investigation of these species is a very challenging task because of their high reactivity and, hence, extreme instability.

During the last years, core hole spectrosopies using synchrotron radiation, including extended X-ray absorption fine edge spectroscopy and X-ray absorption near edge spectroscopy (EXAFS/XANES), X-ray emission spectroscopy (XES), and resonant inelastic X-ray scattering (RIXS), showed their great utility to study the state of iron in various systems. Much effort was directed to the understanding of the iron state in the heterogeneous catalysts[21] and model iron complexes supported by porphyrinic[22,23] and nonporphyrinic[24,25] ligands. On the other hand, advanced computational simulations have been used to predict iron core hole spectra, including XANES[26] and valence to core emission.[27] DFT calculations are particularly useful to predict the properties of intermediate putative species, which are hard to isolate experimentally.[28] Recently, two hypothetical series of iron−oxo and iron−nitrido complexes with iron oxidation states ranging from Fe(IV) to Fe(VI) have been theoretically studied in hydrogen atom transfer reactions.[29]

In our previous study,[30] high-resolution X-ray emission spectroscopy (XES) and resonant inelastic X-ray scattering (RIXS) were applied to study iron species in a series of μ-nitrido diiron phthalocyanines including the initial $[PcFe^{+3.5}NFe^{+3.5}Pc]^0$ and oxidized complexes $[PcFe^{IV}NFe^{IV}Pc]^+PF_6$ and $[PcFe^{IV}NFe^{IV}(Pc^{\bullet+})]^{2+}Br_2$ as model compounds for the intermediates in the catalytic cycle. XES spectra of the Kβ line showed the changes in the spin state between the initial $[PcFe^{+3.5}NFe^{+3.5}Pc]^0$ (LS), one-electron-oxidized $[PcFe^{IV}NFe^{IV}Pc]^+PF_6$ (HS), and two-electron-oxidized cation radical species $[PcFe^{IV}NFe^{IV}(Pc^{\bullet+})]^{2+}Br_2$ (LS). We suggested that the main catalytic pathway of oxidation includes two-electron transformation from the LS initial complex to the LS two-electron-oxidized $[PcFe^{IV}NFe^{IV}(Pc^{\bullet+})(O)]^0$ to generate a powerful oxidant able to oxidize methane via a two-electron process.

In the present work we provide an account of the iron core hole XES and XAS study of the nonsubstituted phthalocyanine μ-bridged diiron complexes containing oxygen, nitrogen, and carbon bridging ligands. The experimental data are compared to the DFT simulations. Then DFT-calculated electronic properties of hypothetical putative oxo complexes formed from the three dimers by adding terminal oxygen to an iron atom were compared. On this basis, particular properties of the N-bridged diiron complex are discussed.

2. EXPERIMENTAL SECTION

2.1. Synthesis and Characterizations. Iron(III) phthalocyanine chloride (FePcCl, 95% purity) obtained from Sigma-Aldrich was purified by the treatment with concentrated HCl to remove impurities and to transform the traces of μ-oxo dimer to FePcCl. Then the product was washed with water until neutral pH and dried. N-Bridged diiron phthalocyanine complexes [PcFeCFePc] (**1**),[18] ([PcFeNFePc]^0 (**2**),[8b] and [PcFeOFe(Pc)] (**3**)[31] were prepared according to published protocols. Their spectroscopic properties were the same as those published in the literature.

X-band (9.5 GHz) EPR spectra were recorded at 77 K on a Bruker ESP 300E spectrometer using a standard rectangular (TE102) EPR cavity (Bruker ER4102ST). Microwave power of 1.6 mW and modulation amplitude of 1 G were used. For quantitative analysis, the EPR spectra were simulated and the experimental spectra were fitted using EasySpin software.[32]

2.2. X-ray Emission and Inelastic Scattering Experiments. The experiments were performed on the high-brilliance X-ray emission beamline ID26 at the ESRF. The electron energy was 6.0 GeV with a ring current of 170−200 mA. The incident flux was 10^{13} photons/s in a 0.2 × 1.5 mm^2 beam footprint on the sample. Two u35 undulators were used to perform the measurements. To detect the inelastic X-ray scattering the sample pellet was aligned to the X-ray beam at 45°. The incident X-ray energy was selected by a pair of Si crystals cut in (220) orientation. The beam was focused in a spot (350 × 60 μm^2) on the sample. The scattered X-rays were monochromatized by the (531) Bragg planes of a spherical bent Si crystal and focused on an avalanche photodiode (APD). When scanning the energy of the scattered X-rays, the APD detector and the spherical bent Si crystal were moved concertedly in order to keep the beam spot on the sample, with the bent crystal and the detector on a Rowland circle, giving an overall resolution taken from the full width at half-maximum of the elastic peak of 0.8 eV. A helium bag was fixed between the sample, the analyzer crystal, and the detector, in order to minimize the absorption of the X-rays by air. To calibrate the energy, we compared all the spectra to an iron foil reference, setting the first inflection of the metallic iron K jump to 7111.8 eV.

To detect the X-ray absorption near-edge structure (XANES) by means of resonant inelastic scattering, the first nonresonant emission spectra were measured and then the emission energy was fixed either at the maximum of the K$\beta_{1,3}$ or the Kβ' emission line and the incident energy was scanned. The spectra are all calibrated to the incident energy scale using the elastic peak measured at the same time as the XES spectra. To determine the position of the main and satellite

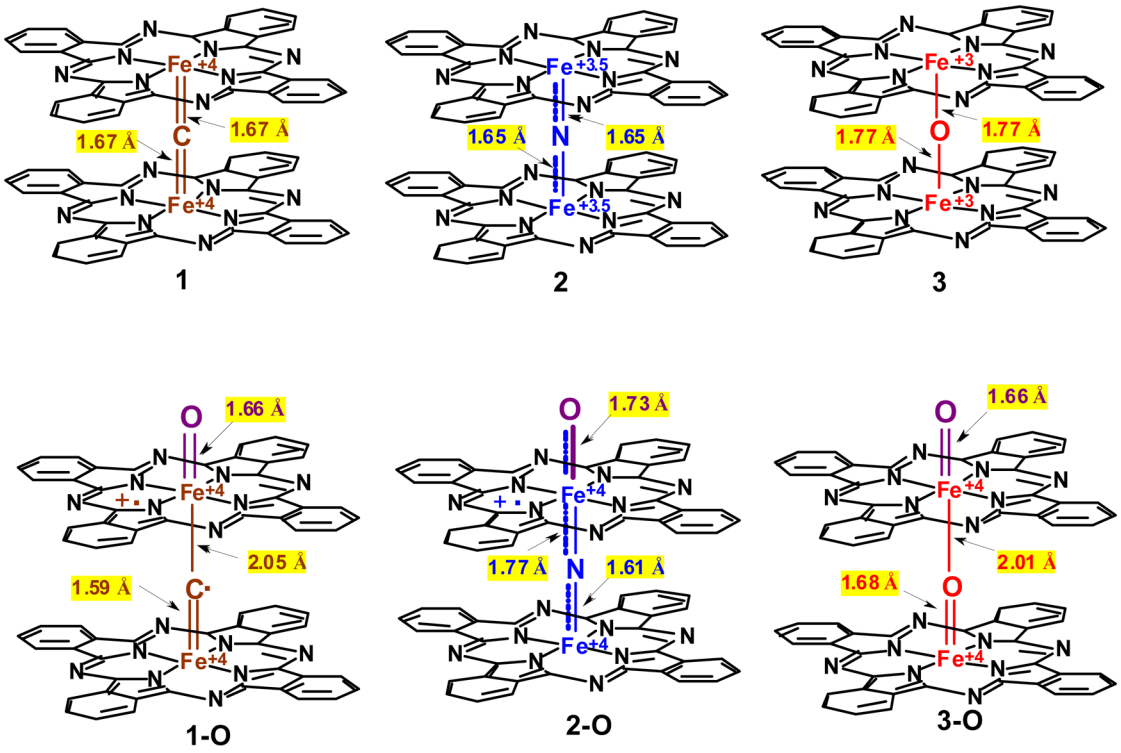

Figure 1. Schematic representation of the DFT structures of the complexes **1**−**3** and their hypothethical oxo species **1-O**−**3-O** with indication of the most importance bond lengths. The structural features of **1**−**3** determined by EXAFS measurements and DFT calculations are identical.

emission line, a Kβ emission spectrum (XES) was recorded first under nonresonant conditions, with an incident energy above the Fe K-edge at 7160 eV. Each scan had duration of 30 s to 2 min, depending on the radiation damage on the samples. For the normalization purposes, EXAFS spectra were recorded on the K$\beta_{1,3}$ and the Kβ' emission line and XANES spectra were normalized to the edge jump in the EXAFS scans. Iron content in the samples was 0.3−0.5 wt % Fe. Comparison of the transmission and fluorescence spectra of such samples showed previously that no substantial difference due to self-adsorption exists at this level of iron contents in the near edge Fe K region.

In order to minimize radiation damage, the samples were cooled to 20 K, and the position of the beam on the sample was changed between the scans. In order to be sure that the X-ray beam did not destroy the iron species under study, we checked for the absence of radiation damage during the exposure time. Prior to every measurement, 30 XANES scans were performed, each 30 s in length. The absence of evolution in the series of the subsequent XANES spectra was a criterion of stability under the beam.

The XES experimental spectra have had the background subtracted by fitting the Kβ main peak with four Voigt peaks, providing a close fit to the Kβ main line and the Kβ valence-to-core spectral background. The spectra are all calibrated to the incident energy scale using the elastic peak measured at the same time as the valence-to-core XES spectra. To treat quantitatively the XANES and XES spectra, the spectra were represented as superpositions of Voigt or Pearson VII amplitude functions, using PeakFit software by Jangel. Areas of the pre-edge features were compared for the spectra normalized to the unity main jump.

2.3. EXAFS Experiments. The EXAFS and conventional XANES spectra were recorded on the SAMBA beamline at the SOLEIL synchrotron (Gif-sur-Yvette, France), operating at 300 mA, 2.75 GeV. The spectra were collected in the transmission mode at the Fe K-edge with a sagittal focusing double crystal Si(220) and focusing mirrors graded at 5 mrad to remove the harmonics. The beam spot was slightly defocused to prevent beam damage to the sample. To compare the pre-edge energy, a metallic Fe foil reference was applied. The first inflection point of metallic Fe was observed at 7111.8 eV. The data were treated with FEFF[33] and VIPER[34] programs. The edge background was extracted using Bayesian smoothing.

The EXAFS spectra were simulated using the FEFF6 program. The DFT-optimized structures were taken as an initial guess, and with the full multiple scattering, the radius 4.5 Å was applied. Then to adjust the simulated spectra to the experimental ones, EXAFS fitting was carried out using as variables the energy shifts and the Debye−Waller parameters as well as slight variations of the interatomic distances (allowed in the range ±0.03 Å). EXAFS fitting was carried out for the first five coordination shells, while molecular bonding topology was fixed. Multiple scattering was taken into account, on the basis of path contributions estimated by FEFF, which are particularly important for the linear fragments of the structure. The parameters of the multiple scattering paths were constrained to be simple arithmetical functions of the corresponding parameters of the related single scattering paths.

2.4. DFT Calculations. In our DFT simulations we followed rather closely the approach developed earlier by Neese and co-workers,[27] which proved to be successful in the representation of core hole spectra of transition metals. All calculations were performed with the ORCA 2.8 software.[35] Geometry optimizations were performed using the generalized gradient approximation (GGA) BP86 functional,[36] with the relativistically recontracted basis set def2-TZVP.[37] To check the validity of the results, calculations with hybrid functionals B3LYP[38,39] and OLYP[40] were carried out for selected species. Full molecular structures were applied with the same basis for all light atoms, but finer grid and larger basis were applied for the iron atoms (see the Supporting Information for the input files headings). The resolution of the identity RI[41] (for BP86) and RIJCOSX[42] (for B3LYP and OLYP) approximations was used to accelerate the calculations. The charge on the complexes was compensated with the dielectric screening model (COSMO). The ORCA flipspin feature has been used to estimate the broken symmetry solutions for the high-spin species.[43,44] Exchange coupling constants were computed with the Yamaguchi formula.[45]

The Fe K core hole XES and XAS spectra of all complexes were calculated using DFT-optimized geometry. As has been shown earlier, the emission and XAS energies calculated by DFT should be shifted by a constant value, depending on the applied functional.[46] The emission

dx.doi.org/10.1021/ic501463q | Inorg. Chem. 2014, 53, 11517−11530

spectra and XAS pre-edges were also calculated with FEFF multiple scattering code, for comparison. Molecular orbitals were visualized using Gabedit software.[47]

3. RESULTS AND DISCUSSION

3.1. Molecular Geometry Determined by EXAFS and DFT Optimization. The series of single atom bridged (μ-X; X = C, N, O) transition metal phthalocyanines $(MPc)_2X$ has been prepared and extensively studied earlier.[7] The nature of the X bridging atom determines the interaction between the metal sites and the extended π-systems of adjacent Pc macrocycles, which in turn defines their catalytic, magnetic, photovoltaic, and electric conductivity properties and other properties important for the applications.

Prior to any discussion of the electronic properties, a reliable structural analysis is necessary. There are no X-ray structures available for the nonsubstituted phthalocyanine compounds under study, because of their insufficient solubility in all common solvents. Meanwhile, due to the absence of substituents, leading to a stronger interaction of macrocycles and closer packing of the molecules in the corresponding solids, nonsubstituted compounds might have advantageous properties for various applications. The results of X-ray determinations for some relevant substituted compounds for which single crystals could be obtained show the presence of the symmetric linear Fe−X−Fe (X = N, C) fragment in the μ-nitrido and μ-carbido complexes, whereas in the μ-oxo complexes the Fe−O−Fe fragment can be quasilinear or bent.[31,48,49] To access the geometry parameters of the molecules **1**−**3**, we determined the molecular geometry from the combined results of DFT calculations and Fe K edge EXAFS measurements (Figure 1, Table 1).

Table 1. Relevant Molecular Geometry Parameters of the Compounds 1−3, Obtained by BP86 DFT Optimization and by EXAFS Fitting

geometry parameter	**1** (carbido)	**2** (nitrido)	**3** (oxo)
d(Fe−X) DFT[a]	1.67	1.65	1.77
d(Fe−X) EXAFS	1.66(2)	1.64(2)	1.76(2)
d(Fe−N) planar DFT	1.95	1.97	1.98
d(Fe−N) planar EXAFS	1.96(3)	1.97(3)	1.97(3)
α(X−Fe−N) DFT[b]	97.4	99.7	100.0

[a]Distances in Å. [b]The corresponding values of angles cannot be reliably addressed by EXAFS.

There are no obvious reasons why the structures of the nonsubstituted dimers should be qualitatively different from those of the substituted counterparts. Therefore, for the initial guess of the DFT optimization we applied the molecular structures of the known substituted phtalocyanine or similar porphyrin compounds.[50,51] Full DFT UKS optimization using the BP86 functional for **1**−**3** leads to geometries with a slight outward distortion of the Pc rings and a displacement of Fe atoms out of the Pc planes toward the bridging atom at 0.252, 0.328, and 0.343 Å for **1**, **2**, and **3**, respectively. There are significant variations of the Fe to central X ligand distances (X = C, N, O) with the Fe−O distance being the longest (1.77 Å) and Fe−N the shortest (1.65 Å). Surprisingly, the Fe−C distance of 1.67 Å in **1** was longer than the Fe−N distance in **2**. The macrocycles are staggered with the dihedral angle N−Fe−Fe−N of 33.6°, 32.2°, and 30.5° for **1**, **2**, and **3**, respectively. The overall molecular topology is similar for three complexes and is exemplified by the case of μ-carbido complex **1** in Figure 2. Beside BP86, B3LYP and OLYP functionals have been tried for geometry optimization. In all instances the singlet states for **1** and **3** and the doublet state for **2** had the lowest energy. The BP86 functional give the best correspondence of key geometry parameters of **1**−**3** to those in similar known compounds with resolved crystalline structure (Tables S1−S3, Supporting Information). Thus, for **2**, BP86 optimization predicts a symmetric geometry with Fe−N distance near 1.65 Å, close to that observed in similar dimers, whereas hybrid B3LYP functional predicts asymmetrical molecules with considerably longer Fe−N bonds. Moreover, BP86 calculation predicts **2** (spin state $S = {}^1/_2$) to have its spin density entirely localized on iron (Table S2, Supporting Information), in agreement with its experimentally observed axial ESR signal having no signs of hyperfine splitting on nitrogen (Figure S1, Supporting Information). By contrast, B3LYP predicts an asymmetric Fe−N−Fe fragment geometry and puts a considerable spin density on nitrogen (Table S2, Supporting Information), which contradicts the experimental observations. OLYP calculations give intermediate results, closer to the BP86 predictions.

Simultaneously with the DFT optimizations, the molecular structure of **1**−**3** was accessed by EXAFS in the solid state. Though the molecular geometry in the solid state might be somewhat different from that of an isolated molecule due to the forces acting upon molecular packing, we assume that such differences are only slight and that the molecules are not

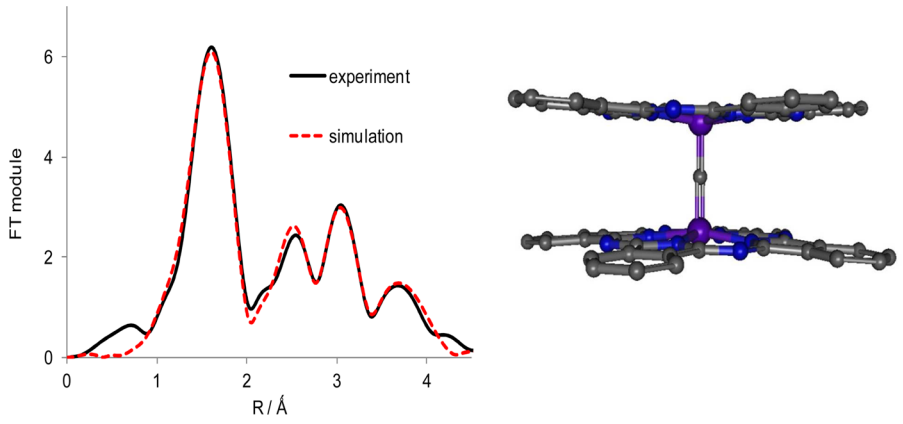

Figure 2. (a, left) Fourier transforms of Fe K EXAFS spectrum of carbido dimer **1** and its FEFF simulation (the first feature below 1 Å is an artifact due to imperfections of baseline correction). (b, right) Overall view of the molecular geometry; hydrogen atoms are omitted.

dx.doi.org/10.1021/ic501463q | Inorg. Chem. 2014, 53, 11517−11530

strongly distorted in the solid state. Such an assumption follows from small differences commonly observed between the geometry of molecules in the gas phase and in the crystallite state.[52]

In order to determine molecular geometry from EXAFS spectra, we started from the DFT-optimized structures. The number of parameters in the molecular structure is too large to allow straightforward fitting. Indeed, even if all multiple scattering (MS) paths are rigidly related to simple scattering ones, for six shells we obtain the number of fitting parameters $P = 24$. For a large window k from 4 to 14 and R from 1 to 5 Å, the number of independent points ($N = \Delta k \Delta R/\pi + 2$) is around 30. The number of freedom degrees ($\upsilon = N - P$) is therefore only 6, which is by far insufficient for statistically significant fitting such complex spectra. Separate fitting of the first shell is also impossible, since the second shell is at relatively close distance, and therefore, it interferes significantly with the first-shell intensities.

To achieve fitting, we allowed only small variations in the most important interatomic distances, such as Fe−X and in-plane Fe−N_p, whereas the lengths of all the MS paths were calculated using simple geometric relationships. Thus, for example, the length for the Fe−C−N three-leg path, which describes the scattering from the closest in-plane nitrogen and the adjacent carbon atom, was represented as the sum of the length of a variable Fe−N_p bond distance and a fixed C−N double bond distance. The differences of the interatomic distances between EXAFS and BP86 DFT geometry optimization results were always smaller than 0.03 Å. This distance variation range seems to be a reasonable minimal estimate, because the precision of the DFT geometry optimizations is usually near this value. Such a fitting approach together with adjustment of the Debye−Waller factors and energy shifts allowed reliable reproducing of the EXAFS spectra. Figure 2a exemplifies the results of EXAFS fitting by an R-space fit of **1**. Similar figures for **2** and **3**, including fitting in R- and k-space and a table of fitting parameters, are given in the Supporting Information (Figure S2 and S3 and Table S4).

An unexpected trend was observed in both DFT optimizations and EXAFS of the variation of the Fe−X distances in the sequence Fe−O > Fe−N < Fe−C, whereas from the formal Lewis structures and bond orders of Fe−X bonds a monotonous decrease of the Fe−X distance should be expected in the series Fe−O (single) > Fe−N (one and a half) > Fe−C (double). The working hypothesis explaining such variation might consider the redox non-innocence of the μ-carbido ligand, leading to the back-donation to the Fe−X antibonding π orbitals. As a result, the following resonant structures might represent the state of the axial carbon in the μ-carbido complex **1**.

$$\mathrm{Fe(IV)}{=}\mathrm{C}{=}\mathrm{Fe(IV)} \leftrightarrow \mathrm{Fe(III)}{-}\mathrm{C}{:}{-}\mathrm{Fe(III)} \quad (1)$$

Note that with respect to μ-carbido complex **1**, it is the only structure among **1**−**3** showing the propensity to partial oxidation with iodine, leading to the formation of conducting solids.[53]

To check whether the trend observed in DFT is not an artifact dependent on the applied functional, we carried out geometry optimization using hybrid B3LYP and OLYP functionals, having a different part of the Hartree−Fock exchange correlation component (see key results in Tables S1−S3 and the MO isosurfaces in Figures S4−S7, Supporting Information). The order of Fe−X distances in the series **1**−**3** was the same, whatever the functional. The Mayer Fe−X bond orders in the optimized structures were 1.47, 1.51, and 1.49 for Fe−C in **1**; 1.64, 1.58, and 1.65 for Fe−N in **2**; and 1.23, 1.16, and 1.21 for Fe−O in **3**, respectively, for BP86, B3LYP, and OLYP functionals (Table S5, Supporting Information). Rather strikingly, μ-nitrido dimer **2** has the highest bond order among the three compounds, higher than its formal value of 1.5, whereas the μ-carbido complex **1** has its Fe−C bridging bond order significantly lower than a formal double bond. Arguably, the order of bonding between two distant iron atoms may be interpreted as a measure of overall covalence in the Fe−X−Fe fragment. The Fe−Fe bond order (from BP86) was 0.45, 0.67, and 0.36 in **1**, **2**, and **3**, respectively, indicating stronger covalence in the nitrido dimer. This qualitative result does not depend on the functional applied (Table S5, Supporting Information).

Overall, good agreement has been obtained between the BP86 DFT geometry optimizations and the EXAFS experiment with respect to key geometry parameters of the complexes **1**−**3**. Besides establishing geometry parameters, we obtain solid evidence that the calculations presented here reliably describe the actual electronic structures of the species under study. Moreover, the calculations on the same level of theory might be extrapolated to the related species which have not yet been observed experimentally.

3.2. Electronic Properties of the Dimeric Complexes According to the Results of Core Hole Fe K Spectroscopies. In this section, we discuss the emission and absorption spectra of **1**−**3** at the Fe K edge. The contributions of oxidation degree and spin state to the spectral features are discussed. Core hole spectroscopies can straightforwardly probe the electronic state of the transition metal ions in the complexes, which is not available by other physical techniques. Thus, according to the EPR measurements, both μ-oxo and μ-carbido complexes are EPR silent, whereas **2** and substituted μ-nitrido diiron complexes similar to **2** show a strong axial signal, typical for low-spin iron (Figure S1, Supporting Information).[12,13] In dimeric iron species, states of different multiplicity but the same orbital configuration are possible. For this reason, the local spin density on the iron atoms of the dimeric species might be not accessible by EPR but can be probed by core hole spectroscopy. On the other hand, the oxidation state of iron can be deduced from the XAS pre-edge features. When detected using resonant inelastic X-ray scattering (RIXS), the pre-edge features become also diagnostic for the spin states of the central Fe atom, since the final state has p-symmetry and interacts with the partially filled d-levels.

3.2.1. Kβ Main Line Emission Spectra (3p−1s Transitions) and Spin States of 1−3. For the first row transition metals, K-edge X-ray emission spectroscopy (XES) can be efficiently used to determine the metal spin state. The intermediate state contains an electronic state with a 1s core hole, and the final state is reached when the 1s vacancy is filled, creating a 3p hole. Therefore, the Kβ (3p → 1s) line involves a p-symmetry core hole in the final state. The final state interactions between the 3p core hole and the partially filled 3d band explain the sensitivity of the XES spectra to the metal spin.[54−56] The Kβ line is split into several multiplet states determined by Coulomb and exchange interactions, leading to the appearance of satellite features.

A simple rationale of the influence of exchange interaction on the emission spectra was proposed by Tsutsumi et al., who demonstrated for the first row transition metals that the energy

dx.doi.org/10.1021/ic501463q | Inorg. Chem. 2014, 53, 11517−11530

difference between the K$\beta_{1,3}$ and Kβ' lines is approximately equal to $J(2S + 1)$ and that the Kβ' to the K$\beta_{1,3}$ intensity ratio could be correlated to the ratio between final state multiplicities $S/(S + 1)$, where S is the spin of the 3d shell and J is the exchange integral.[57]

The Kβ spectra of three compounds under study are given in Figure 3. The μ-nitrido dimer **2** shows the Kβ' feature merged

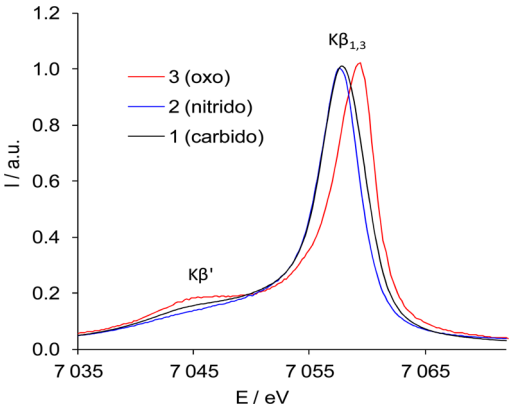

Figure 3. Main Kβ emission spectra of complexes **1**–**3**.

to the K$\beta_{1,3}$ one, therefore being undistinguishable. The μ-oxo dimer **3** demonstrates a separated Kβ' peak typical for high-spin species, whereas μ-carbido complex **1** shows a spectrum intermediate between those of **2** and **3**. The emission spectra of **2** and **3** are in agreement with their previously reported low-spin state for **2** and antiferromagnetically coupled high-spin state of iron for **3**. Although μ-carbido dimer **1** is EPR-silent and supposed to be a closed-shell compound, it shows an unexpected increase of the Kβ' intensity. This might suggest a non-innocence of the μ-carbido bridging ligand, as discussed in the previous section. Being formally in the sp hybdridization state, carbon provides two electrons for π-bonding with iron. However, electron withdrawing by Fe(IV) (d^4) leads to delocalization of the electron from carbon onto the d-orbitals and partially stabilizes high-spin states in the d^5 manifold. As carbon p-orbitals are higher in energy than nitrogen ones, the resonance described by eq 1 is more important for **1** than for **2**, which, however, does not lead to the formation of observable paramagnetic species of **1**.

As proposed by Glatzel et al.,[58] the first moment M1 of the Kβ main emission spectrum is an adequate parameter to estimate the oxidation state. The first moments of the K$\beta_{1,3}$ emission peaks are 7057.75, 7057.45, and 7058.32 eV for **1**, **2**, and **3**, respectively; i.e., the highest oxidation degree should be attributed to **2** and the lowest to **3** and the complex **1** has an intermediate state. While the M1 values for **1** and **2** differ only slightly, μ-oxo dimer **3** has a significantly higher M1 and therefore a lower oxidation state, corresponding to Fe(III).

Recently, Pollock et al. reconsidered the main line interpretation as a probe of metal–ligand covalency. Restricted active space CI calculations using QROs generated by conventional DFT allowed one to estimate the covalency (from the QROs coefficients) and to calculate main emission lines. It has been concluded that for a given formal oxidation state of iron, the increase of covalency leads to a reduction of the main line splitting.[59] The magnitude of such an effect might be comparable to the effect of d-electron count. If interpreted in the light of the insights given in ref 59, our experimental results suggest the highest covalency in **2**, particularly taking into account that the effect of d-electron count should go in the opposite sense, i.e., to give lesser separation in **1** than in **2**. Therefore, considering the main line separation further corroborates our conclusion about higher covalency and shorter Fe–N distance in **2**.

Broken symmetry DFT calculations have been carried out to address the possible spin states in the complexes **1**–**3**. Broken symmetry solutions were considered with the multiplicity values supposing the local iron spin $S = {}^5/_2$, ${}^3/_2$, or ${}^1/_2$ on iron atoms for Fe(III) in **1** and **2** or S = 1 or 2 for Fe(IV) in **1** and **2**, with the final value Ms = 0 for **1** and **3** and Ms = ${}^1/_2$ for **2**. The J-values obtained for three functionals and different spin values are summarized in Tables S1–S3 of the Supporting Information. For the complex **3**, antiferromagnetic interaction was found in the case of $S = {}^5/_2$ with J = 239.9, 378.2, and 515.6 cm^{-1}, for B3LYP, OLYP, and BP86, respectively. The J value calculated for **3** using the hybrid functional B3LYP is in good agreement with the values obtained from magnetic data for similar μ-oxo dimers, which are invariably antiferromagnetic with J values in the range 180–230 cm^{-1}.[60] In general, for simulating the antiferromagnetic coupling exchange, the hybrid functionals seem to be more accurate than the GGA functional.[61] For all functionals, however, the broken symmetry solution with S = 5 had the lowest energy among all tried spin configurations and had the same energy as the S = 0 solution. Note that for **3** the S = 0 UKS B3LYP, OLYP, and BP86 calculations using the initial guess of molecular orbitals extracted from the S = 5 one spontaneously converge to the antiparallel spins orientation and the same energy as the BS solution (Figure S10, Table S8, Supporting Information).

Recently, Ghosh and co-workers reported on the advantages of the OLYP functional for the comparison of energies of different spin states of iron complexes.[62] Our OLYP single-point energy broken-symmetry calculations for **3** (S = 5, Ms = 0) were carried out on the geometries optimized with BP86 or OLYP itself (Table S3, Supporting Information). OLYP suggests stronger overlap in the antiferromagnetically coupled orbitals, in agreement with previous works.[63] The results from three functionals are qualitatively identical with an obvious preference for the antiferromagnetically coupled spins for S = 5 and high energies of the BS solutions for lower values of total spin. However, OLYP and BP86 predict the J values out of the range observed experimentally for the Fe–O–Fe antiferromagnetically coupled moieties.

The open-shell solutions for μ-carbido dimer **1** all have much higher energy than the closed-shell ground state, and the broken-symmetry solutions with Ms = 0 systematically converge to the closed-shell state with no residual spin density, giving unphysical values of J (Table S1, Supporting Information). Similarly, in the μ-nitrido dimer **2** all high-spin configurations have high energies and converge to the same low-spin $S = {}^1/_2$, Ms = ${}^1/_2$ solution (Table S2, Supporting Information). Therefore, our broken symmetry calculations agree with the observed differences of the XES main line, interpreted as being due to the variations of the local iron spin in **3** and (**2**, **1**). However, the BS calculations failed to account for small difference of spectra between **1** and **2**. The last difference is probably due to the higher covalence of **2** rather than to spin states, in agreement with a recent paper by Pollock et al.[59]

It should be pointed out that correct spin density distributions are difficult to obtain within the standard

dx.doi.org/10.1021/ic501463q | Inorg. Chem. 2014, 53, 11517–11530

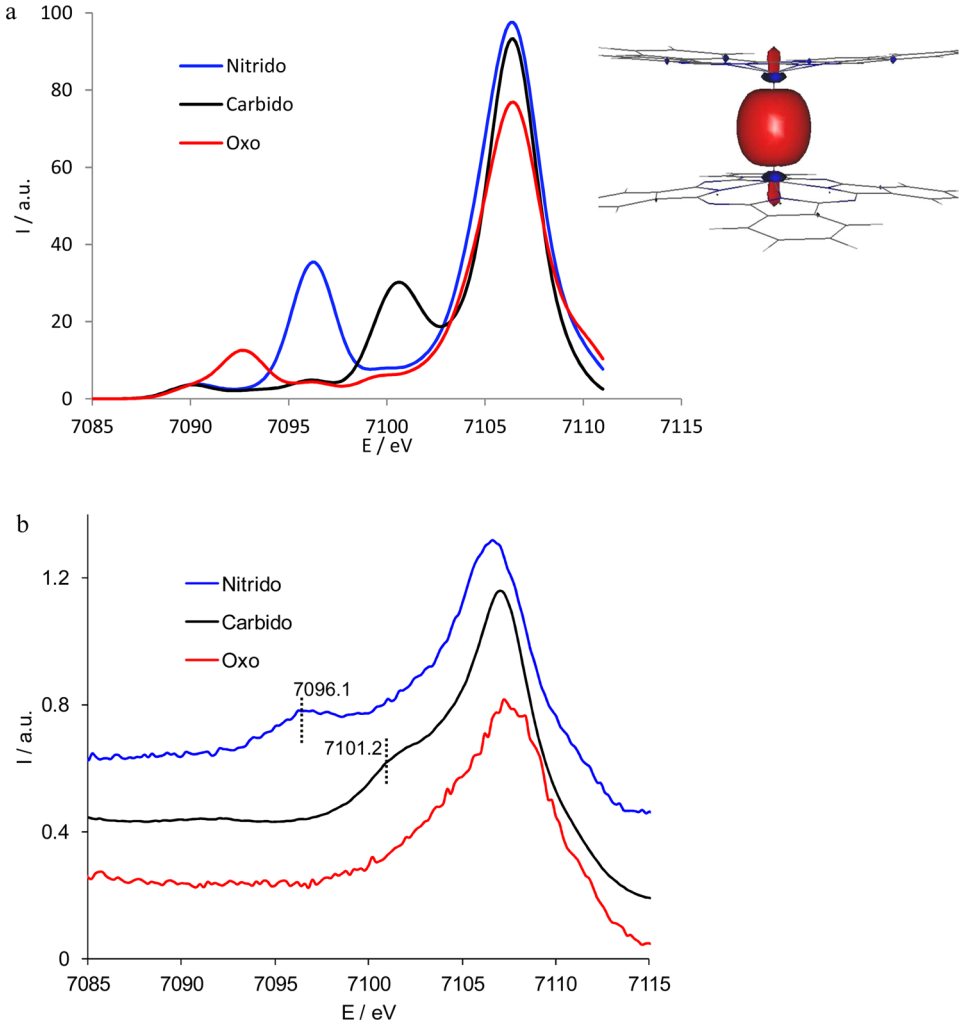

Figure 4. DFT calculated (a) and experimentally observed (b) valence to core emission spectra of the dimers **1**−**3**.

Kohn−Sham formalism. Obtaining reliable spin density distributions is important for the calculation of properties, but this task remains difficult to achieve for theoretical chemistry.[64,65] Single-determinant high-spin and broken-symmetry calculations have been successfully applied to the open-shell d-metals systems.[66] However, this approach has serious pitfalls, since a spin pure wave function can be represented by a single determinant only for the highest spin state. The BS states having spin projection values below the maximum value are spin-contaminated and are appropriate to evaluate spin-state energies only. The most valuable approach to reliably compare spin states is undoubtedly the CI calculations, but for such molecules as **1**−**3** it remains beyond our calculation possibilities. However, the ensemble of the experimental data and the results of UKS and broken symmetry calculations provide a coherent picture for **1**−**3**.

In summary, the main line Kβ emission spectra show the presence of high-spin atiferromagnetically coupled Fe(III) sites in **3** and low-spin Fe states in **2**, in line with the relative energy of the broken-symmetry DFT solutions. The shortest Fe−X bond distance for **2**, obtained by a combined DFT−EXAFS study, agrees with its low-spin state. According to both XES data and DFT calculations, the covalency of the Fe−C bond in the μ-carbido complex **1** seems to be lower than the Fe−N bond covalency in **2**, probably due to a contribution from the resonance structure (eq 1).

3.2.2. Valence to Core Emission Spectra. These transitions have been assigned as ligand np to metal 1s and ligand ns to metal 1s, otherwise called "satellite" transitions.[67] While the Kβ main lines are dominated by spin-state contributions, the valence to core region has greater sensitivity to the changes in the oxidation state and coordination mode. The valence to core emission spectra proved to be particularly useful for the identification of light ligands in the miltinuclear metallic clusters.[68] At the same time, a lower intensity (ca. 100 times lower than for the main line) requires much longer acquisition time, which sometimes is incompatible with the stability of samples to the radiation damage.

The observed valence-to-core transitions of **1**−**3** are different and obviously sensitive to the ligand environment of the iron center. The background-subtracted measured and calculated spectra are shown in Figure 4 with a broadening parameter of 1.5 eV to simulate the broadening effects in the calculated spectra. All three spectra have similar high-energy valence-to-core parts. Additionally, the Kβ'' or "crossover" peak at lower fluorescence energies could be distinguished for μ-carbido **1** and μ-nitrido **2** complexes, at 7101.2 and 7096.1 eV, respectively. By contrast, for the μ-oxo dimer **3**, no crossover peak but only the K$\beta_{2,5}$ lump near the Fermi level was observed.

dx.doi.org/10.1021/ic501463q | *Inorg. Chem.* 2014, 53, 11517−11530

The crossover (or Kβ'') peak in the transition metal complexes was assigned to ligand 2s to metal 1s crossover transitions. A strong (exponential) dependence of crossover intensity on the metal to ligand distance was demonstrated.[63]

Therefore, we suppose that the presence of a crossover peak in **1** and **2** is due to the presence of short bonds with carbon and nitrogen ligands, respectively. As the position of the crossover feature depends on the binding energy of the ligand 2s orbital, it can be used to identify the nature of the ligand.[69] Qualitatively, since carbon s-orbitals are higher in energy than those of nitrogen, the carbon crossover feature for **1** should be expected at nearly −5 eV relative to the energy of the crossover peak of **2**. Indeed, when carbide and nitride ligands are simultaneously present in a material, their XPS 2s peaks are separated by approximately 5 eV.[70]

DFT calculations were applied to simulate the experimental valence to core spectra and to evaluate the contributions of valence orbitals to the experimentally observed intensities. The DFT calculation allows reproduction of the position of the experimentally observed crossover peak for the cases if the ligand stays at a short distance, i.e., only for the bridging ligands in the Fe−X−Fe fragment. As illustrated by Figure 4, the molecular orbitals contributing to the intensity of crossover peaks have predominantly s-character. In contrast to position values, the crossover peak intensities cannot be calculated, as their intensity depends on the convolution width, adjusted arbitrarily. In the experimental spectra, the lines are strongly broadened by miltiplet interactions, which are not taken into account by DFT. If for **1** and **2** the valence to core spectra unambiguously indicate the presence of different axial ligands, the crossover peak of **3** predicted by DFT could not be observed experimentally, probably because of its lower intensity and greater width. Similarly to the case of the main valence to core peak, it shows a broad feature consisting of many transitions with close energies, and its reliable interpretation seems difficult. Beside the crossover peaks for **1** and **2**, the valence-to-core spectra of **1**−**3** were quite similar. Multiple scattering code FEFF8.2 also reproduces the crossover peaks at the right positions (Figure S11, Supporting Information), but with physical interpretation of the features, they are not clear in this case.

3.2.3. Pre-Edge and Main Jump Features of XAS Spectra. The position and the intensity of the Fe K XAS pre-edge peak are diagnostic of the electronic structure and geometry of iron species. Since only few transitions contribute to the pre-edge intensity, as compared to the main jump, simple interpretation of the observed data is often possible. The pre-edge energy is expected to increase as the iron atom oxidation degree and the ligand field strength around the iron atom increase. An increase of the pre-edge energy by nearly 1 eV per unit change in the oxidation degree is commonly observed.[24b,71] However, changes of the site symmetry and the nature of the ligands might cause significant variations of the pre-edge energy within the same formal oxidation degree. High-valent iron species often show more intense pre-edge features than lower-valent counterparts due to the presence of a greater number of vacant d-orbitals. In addition, for μ-nitrido iron species, an increase of the pre-edge intensity comes from the presence of short Fe−N bonds, which distort the site symmetry and provide a mechanism for 3d−4p mixing, thus increasing a dipole-allowed pre-edge intensity.[30] The experimental XANES spectra of **1**−**3** are presented in Figure 5. The energy of main jump changes in the sequence **1** > **2** > **3** is in agreement with the expected

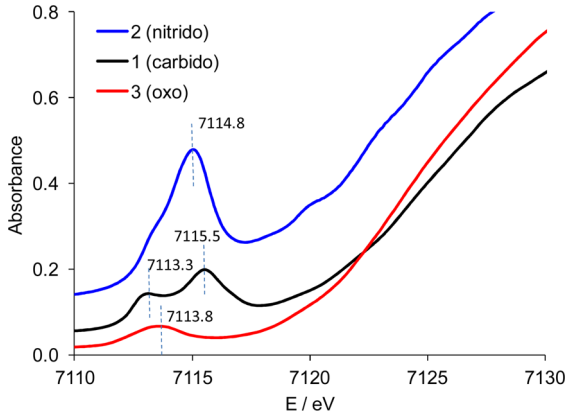

Figure 5. Experimentally observed pre-edge and main jump XANES spectra for the dimers **1**−**3**.

variation of iron oxidation state in the same sequence. The maximum of derivative observed in the XANES region was at 7123.6 eV (**1**), 7122.5 eV (**2**), and 7121.95 eV (**3**). The positions of the pre-edge maxima also qualitatively agree with the expected order **1** > **2** > **3**. The highest pre-edge intensity was observed for **2** and the lowest for **3**.

Detailed analysis of the pre-edge features was achieved with the RIXS technique. It allows distinguishing between the high- and low-spin states due to the unequal probability of spin-up and spin-down intermediate states in the cases when resonance scattering occurs on K$\beta_{1,3}$ and Kβ', respectively. Since the Kβ' line represents the antiparallel orientation of spin between the 3p hole and 3d shell, for high-spin iron sites there should be no XANES pre-edge observed under resonant conditions at the Kβ' emission energy. This allows measuring spin-selective XANES spectra.

To this aim, XANES spectra at the Fe K edge were recorded on the maximum of K$\beta_{1,3}$ emission line (7059 eV) and on the Kβ' line (7045 eV) in order to distinguish between spin-up and spin-down transitions. In addition, the Kβ-detected XANES spectra allow a more precise separation of the weak K pre-edge structure from the main edge as compared to the conventional absorption spectroscopy edge. In our previous work,[30] RIXS was applied to study the spin state in the series of μ-nitrido diiron tetra-*tert*-butylphthalocyanines in three oxidation states: Fe(III)Fe(IV), Fe(IV)Fe(IV), and Fe(IV)Fe(IV) phthalocyanine cation radical. The spectra of nonsubstituted **2** measured here are therefore qualitatively similar to those of μ-nitrido Fe(III)Fe(IV) complex from ref 30, since the corresponding compounds differ only by the presence of *tert*-butyl substituents in the phthalocyanine aromatic rings.

Background-corrected pre-edge spectra of **1**−**3** are shown in Figure 7. Table 2 summarizes the numeric data of the pre-edge fitting using Voigt amplitude functions. The spectra of μ-carbido dimer **1** obtained on two emission energies both show a double maximum, with a somewhat different ratio between the higher and the lower energy. Two components are also present for **2**, but they are not resolved in energy to give the separated peaks. The overall intensities of the pre-edge peaks are much higher for **1** and **2** than for **3**, in agreement with nonresonant XANES, probably due to the presence of shorter Fe−X axial bonds in **1** and **2**. The pre-edge intensity of **1** and **2** is moderately modified by change of the emission energy. Upon decrease of emission energy from 7059 eV down to 7045 eV, the low-energy component in the pre-edge of **1** and **2** remains

dx.doi.org/10.1021/ic501463q | *Inorg. Chem.* 2014, 53, 11517−11530

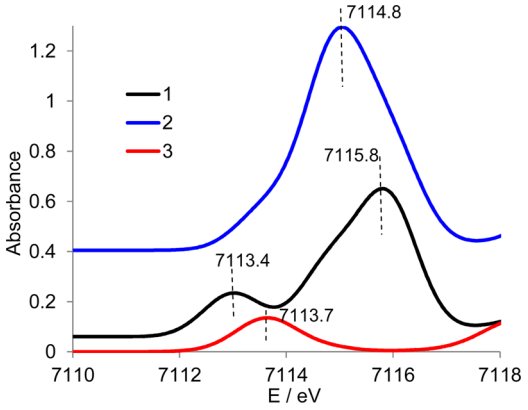

Figure 6. DFT-calculated pre-edge features of the dimers **1**−**3**.

constant, whereas the high-energy contribution decreases significantly (Table 2). This change of intensity could be expected since, in any event, the probability of spin-up and spin-down transitions should be different for a nonzero local spin of d-manifold, even in low-spin systems. This observation indicates as well the presence of nonzero local spin on iron sites for the formally closed-shell μ-carbido complex **1**. More detailed analysis of this issue is beyond the scope of the present work. For the resonant XANES of **3**, the Kβ' fluorescence at the pre-edge energies is almost absent, some residual intensity being rather due to the experimental imperfections. Therefore, the high-spin nature of **3** is confirmed by resonant spin selective XANES.

While the pre-edge energies and intensities provide qualitative insight into the local geometric and electronic state of an absorbing iron site, there are other factors that make it difficult to go beyond a phenomenological interpretation. Therefore, theoretical simulation is necessary to predict pre-edge energies and intensities. The pre-edge simulation methodology by the DFT approach has been developed for a series of ferrous and ferric complexes.[26,27] Here we apply this

Table 2. Parameters[a] of the RIXS XANES Pre-Edge Features for the Complexes 1−3 Measured at Two Different Emission Energies: 7059 eV (K$\beta_{1,3}$) and 7045 eV (Kβ')

sample	K$\beta_{1,3}$	Kβ'
1	7113.3/0.26	7113.2/0.25
	7115.7/0.57	7115.6/0.28
2	7114.5/0.24	7114.7/0.27
	7116.2/0.83	7116.0/0.54
3	7113.8/0.33	7113.8/0.041

[a]Data are presented as energy (eV)/normalized intensity.

protocol to the complexes **1**−**3**. Calculated pre-edge spectra of the complexes are given in Figure 6. The calculated spectra reproduce well the experimental energies and the intensities of the pre-edge transitions in all three complexes. Molecular orbitals and mechanisms contributing to the intensity of the pre-edges were identified, and in all cases the intensities are mostly due to dipole transitions with participation of the orbitals having a strong contribution of the iron d_{z^2} orbitals (Supporting Information, Figure S12).

Similarly to DFT, multiple scattering code FEFF8.2 well-reproduces all the pre-edge spectra features. The drawback of the multiple scattering calculations is the absence of a further rationale for the obtained results, whereas for the DFT calculations the molecular orbitals corresponding to the transitions can be easily identified and visualized.

In Figure S13 (Supporting Information) are presented XAS pre-edge spectra obtained for high-spin and broken-symmetry Ms = 0 solutions for **3** state with multiplicity 11. The position and intensity of the pre-edge peak depend on the antiferromagnetic coupling of the high-spin species. Thus, if both iron atoms have the same (e.g., spin-up) configuration, excitation of a spin-down electron decreases the miltiplicity of the intermediate state, whereas excitation of a spin-up electron on the partially populated d-levels is forbidden and should occur only on the empty ones. By contrast, for antiferromagnetically coupled iron sites, excitation of both spin-up and spin-

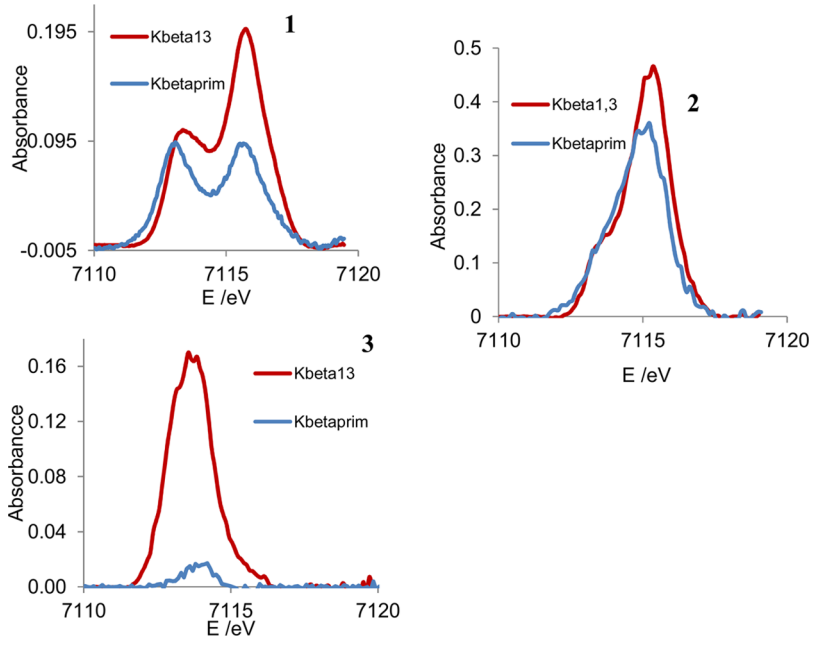

Figure 7. Pre-edge features of **1**−**3** detected at different emission energies.

dx.doi.org/10.1021/ic501463q | *Inorg. Chem.* 2014, 53, 11517−11530

down to partially occupied levels occurs in a symmetric manner, leading to an increase of multiplicity. Moreover, the energy of partially filled d-states is lowered by antiferromagnetic coupling. In this manner, DFT calculations of the XAS pre-edge might be used to determine the spin state in multisite systems.

Overall, XANES spectra confirm the variations of the iron oxidation state from Fe(III) to Fe(IV) in the series **1**−**3** and the difference of spin states of iron sites as deduced in the previous sections. The intensities and energies of XANES pre-edges are reliably reproduced by the DFT calculations. Remarkably good agreement of the simulated pre-edge features with experimental data on the diiron species has been found, allowing one to assign the pre-edge features to the excitations of core electrons into the empty iron d-orbitals, which mix with 4p orbitals.

3.3. DFT Study of the Hypothetical High-Valent Oxo Complexes of 1−3. It is widely recognized that the oxidation of the phthalocyanine and porphyrin complexes occurs via high-valent iron oxo species. In monomeric porphyrin species, these complexes have a Fe(IV)═O unit supported by a ligand cation radical.[4] While a significant number of non-heme oxo complexes were prepared and characterized,[4e,24,72] the oxo species supported by porphyrin[73] and especially phthalocyanine[14] platforms are less documented. These complexes are very reactive and, consequently, very unstable, which makes their preparation and spectroscopic characterization very challenging. For example, the long-sought cytochrome P-450 compound I intermediate was definitively characterized only recently.[74] Apparently, very strongly oxidizing μ-nitrido diiron phthalocyanine oxo species have quite low stability. Despite our numerous efforts to prepare these species[13] by freeze-quenching and to obtain their XAS and XES spectra, no spectroscopic signatures of these putative diiron oxo species were obtained as yet.

The influence of axial ligand on the reactivity of mononuclear high valent iron oxo complexes was studied in many theoretical and experimental works, mainly in relation to the reactivity of cytochrome P450 and its biomimetic analogues.[4,28,75,76] In the single-atom bridged diiron complexes, the nature of the bridging ligand seems to be essential for the catalytic activity.

DFT calculations provide adequate description of the electronic structure and have been extensively benchmarked earlier for iron complexes.[77] As shown in the previous sections, our DFT calculations on the complexes **1**−**3** reliably reproduce their geometry and the features of their core hole spectra. In this section, we make a step forward and extrapolate our BP86 DFT calculations from the extensively characterized **1**−**3** to the experimentally nonidentified but supposedly important oxo intermediates **1-O**, **2-O**, and **3-O**, all containing one additional terminal oxygen connected to an iron atom.

As our efforts to isolate and characterize such species have all failed as yet, DFT-calculated XAS and XES spectra might indicate what we can expect to observe in case of successful isolation of the oxo species and should there be any particular spectral features allowing identifying them. On the other hand, comparison of the properties of putative oxo complexes **1-O**−**3-O** calculated by DFT might be useful to guess the reasons for the observed differences in the catalytic properties of three diiron complexes **1**−**3**.

Documented below are the results obtained from UKS calculations with the BP86 functional. Beside the lower computational cost of BP86, the previous studies showed that while hybrid functionals usually perform better for main-group chemistry, BP86 is often superior for transition metal chemistry. Thus, Barden et al.[78] compared several local and hybrid functionals (LSDA, BP86, BLYP, B3P86, B3LYP) applied to nine homonuclear 3d dimers. For the bond distances the mean unsigned error (MUE) was 0.020 Å for BP86 and 0.053 Å for B3LYP.

To construct the initial models, optimized structures of **1**−**3** were incremented with an oxygen atom, axially bound to one iron atom at the initial distance of 1.7 Å. All well-identified putative oxo intermediates can be considered as the products of two-electron oxidation of iron center by means of donation of an oxygen atom, leading to the formation of a double bond Fe═O.[14] The simulated oxo species are therefore all neutral, as the initial complexes. In the diiron complexes, formation of oxo species with two terminal oxygen atoms could be formally considered. However, taking into account the low stability of the oxo species with even one terminal oxygen, the binding of two oxygens seems less probable, as it should result in four-electron oxidation and such species should be extremely unstable. Thus, only one terminal oxygen atom was observed for the oxo complex of the diiron porphyrin analogue.[6]

Parameters of the optimized geometries and selected Loewdin spin-populations and charges for the complexes **1-O**−**3-O** are given in Table 3. Full results of geometry optimizations are provided in the Supporting Information as *xyz* files.

Table 3. Principal Parameters of Geometry and Electronic Structure of Hypothetical Oxo Complexes 1-O−3-O, Obtained by DFT BP86 UKS Calculations

geometry parameter	**1-O** (carbido)	**2-O** (nitrido)	**3-O** (oxo)
d(Fe−X)[a] in the initial complex	1.669	1.654	1.773
d(Fe−X) in the oxo complex, short	1.59	1.61	1.68
d(Fe−X) in the oxo complex, long[b]	2.05	1.77	2.01
d(Fe═O) in the oxo complex	1.66	1.73	1.66
Q/S(Fe1)[c,d]	0.11/0.00	0.23/0.03	0.35/−1.25
Q/S(Fe2)	0.15/0.00	0.14/0.37	0.26/1.14
Q/S(X)	0.14/0.00	−0.08/−0.14	−0.15/−0.57
Q/S(O_t)	−0.28/0.00	−0.31/0.75	−0.28/0.734
E(HOMO)	−0.18588	−0.18342	−0.18392
E(LUMO)	−0.16499	−0.18084	−0.16680

[a]Distances in Å. [b]Adjacent to the Fe═O fragment. [c]Q = Loewdin charge, S = Loewdin spin. [d]Fe1 is a non-oxygen-bearing iron, Fe2 is an oxygen-bearing iron, and O_t is a terminal oxygen.

Three oxo complexes show a preference for the lowest miltipliciy, i.e., singlet for **1-O**−**3-O** and doublet for **2-O**. Imposing a higher spin multiplicity leads to distorted geometries (Supporting Information, Figure S15) and much higher energies (Supporting Information, Table S6). Addition of terminal oxygen to one of iron atoms leads to the expected loss of symmetry of the Fe−X−Fe fragment with elongation of the Fe−X bond adjacent to the Fe═O terminal bond, whereas another Fe−X bond becomes shorter than in the initial dimer. This effect is very significant for **1** and **3**, but much less for **2**. In **1** and **3**, the formation of an oxo complex leads to breaking of the conjugated π-system of the Fe−X−Fe fragment and to the formation of a long single Fe−X bond (2.01 Å for X = O and 2.05 Å for X = C), whereas the Fe−N bond in **2** is only weakly

dx.doi.org/10.1021/ic501463q | *Inorg. Chem.* 2014, 53, 11517−11530

elongated, from 1.65 to 1.77 Å, indicating stronger covalence in the Fe−N−Fe fragment. Noteworthy, the stabilization of the high iron oxidation state by nitrido ligands has been evidenced previously.[73,79]

The HOMOs of the three oxo complexes are very similar in shape and energy (Table 3 and Supporting Information, Figures S7−S9), all being dominated by the contribution from an a_{1u} π^* orbital of the macrocycle, adjacent to the terminal Fe═O bond. This is in contrast to the HOMO of the initial complexes, which are mostly of 3d Fe character, as exemplified by the case of complex **2** in Figure 8.

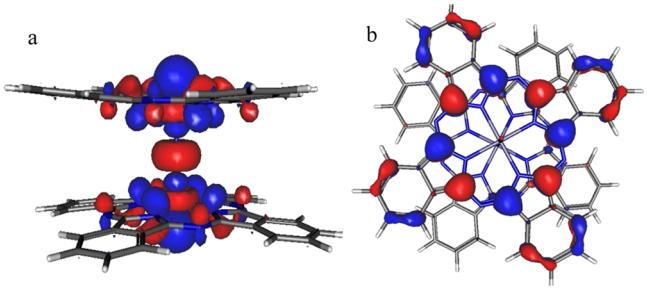

Figure 8. α-HOMO of the μ-nitrido dimer **2** (a) and of the oxo complex of **2** (b).

In this series, only **2-O** has the odd number of electrons and its SOMO (which in the spin-unrestricted calculation corresponds with the β-LUMO orbital) is localized on the Fe−N−Fe═O axial fragment (Figure 9), being correlated with the total spin density (Figure 10).

In this work, we do not consider mechanistic details of catalytic oxidation by high-valent oxo complexes. However, in general terms, comparative reactivity of such high-valent species would depend on the relative energy position and shape of the LUMO frontier orbitals.

For the complexes **1-O** and **2-O**, the LUMOs contain a significant contribution from the Fe═O bond of π^* type as well as from the Fe−X bonding density, whereas for **3-O**, the LUMO has a σ^* character (Figure 9). Therefore, any of these molecules would react with an electron donor with elongation and weakening of the terminal Fe═O bond. Among the three complexes, **2-O** has the longest Fe−O distance of 1.73 Å, the highest spin density on the oxygen atom, and the lowest Fe═O bond order (Figure 10 and Supporting Information, Table S6).

Therefore, we can speculate that more covalent character of the Fe−N bond as compared to Fe−O and Fe−C bonds in the series **1-O**−**3-O** leads to a stronger trans-effect of the bridging nitrogen, which makes **2-O** more prone to dissociate, forming an oxyl radical. The LUMO of **2-O** is placed 10 kcal/mol lower than the corresponding LUMOs of **1-O** and **3-O**, which implies

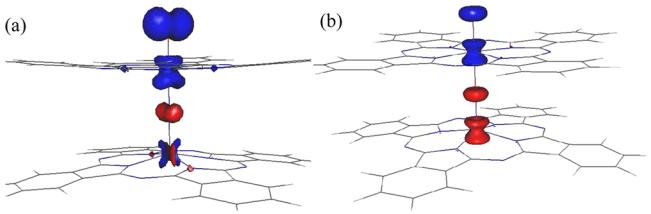

Figure 10. Spin density distribution surface calculated for the $S = {}^1/_2$ ground state of **2-O** (a) and for the singlet ground state of **3-O** (b), at an isovalue of 0.025. (For **1-O**, BP86 UKS calculation converged to a closed-shell solution with no spin density.)

a greater oxidation potential for the μ-nitrido **2-O** (Table 3). As reported by Ye and Neese, the C−H bond activation catalyzed by high-valent iron(IV) oxo species occurs via the transition state involving an oxyl radical.[80] Depending on the bridging ligand, the Fe═O bond length might therefore correlate with the reactivity of high-valent iron oxo complexes.

Such an explanation of thr higher reactivity of **2** should be considered as a preliminary suggestion. Further work in this direction is underway.

The XANES and valence to core XES spectra of **1-O**−**3-O** have also been calculated (Figures 11 and S16 and S17, Supporting Information). For all three complexes **1**−**3** the addition of the oxygen atom leads to the formation of the same type of high-valent diiron species. Upon formation of the oxo complex, the environment of one iron site of the dimer is modified.

The contributions of two iron atoms to the XAS and XES spectra become unequal and should be considered separately, whereas the spectra become superpositions of two contributions. For all three species, the XAS pre-edge feature of the iron site bearing an oxygen atom (top Fe═O, Supporting Information, Figure S16) becomes smaller, since the coordination sphere is symmetrized. The pre-edges spectra of the oxo complexes are dominated by the asymmetrically coordinated non-oxygen-bearing Fe (bottom Fe, Supporting Information, Figure S16). The pre-edge of **3-O** becomes a superposition of contributions from two different Fe(IV) sites. The second iron atom not bond to terminal oxygen forms a short double bond with bridging oxygen and raises its formal oxidation degree from Fe(III) to Fe(IV). Therefore, the oxo species **1-O**−**3-O**, if ever isolated, are predicted to show typical Fe(IV) XANES prepeaks. Overall, for the oxo complexes **1-O**−**3-O**, we expect XANES to be dominated by a non-oxygen-bearing Fe atom, with the shape and energy of the pre-edge similar to that of the oxidized Fe(IV)Fe(IV) species, easily formed in the reaction medium, which makes difficult their eventual detection by XANES. An additional short Fe═O bond might be detectable by EXAFS and crossover valence-to-core XES. Indeed, a novel

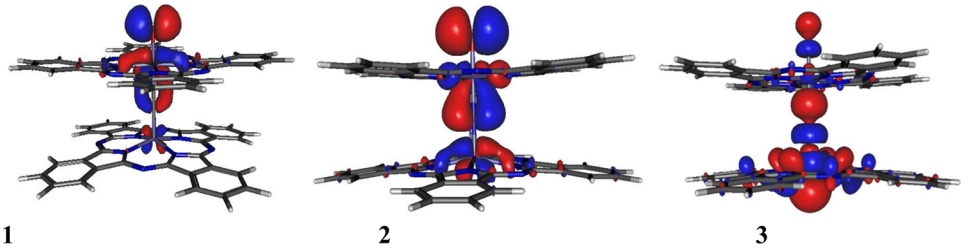

Figure 9. Spin-down LUMO orbitals of the oxo complexes of μ-carbido **1**, μ-nitrido **2**, and μ-oxo **3** dimers at the same isovalue of 0.025.

dx.doi.org/10.1021/ic501463q | Inorg. Chem. 2014, 53, 11517−11530

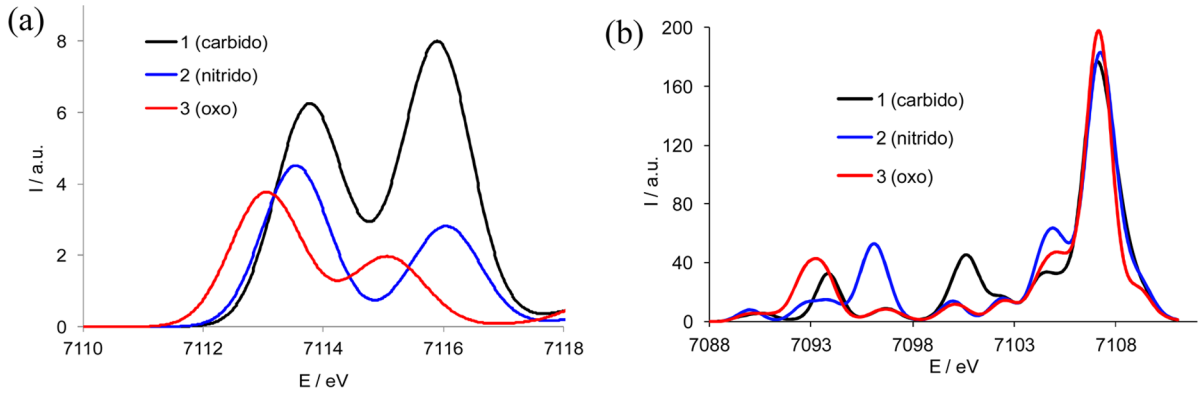

Figure 11. Calculated Fe K XAS pre-edges (a) and valence to core XES (b) for the high-valent oxo complexes **1-O**−**3-O**.

feature due to the Fe═O bond would appear in the **1-O**−**3-O** near 7093 eV, as shown in Figure 11b. Note, however, that in situ acquiring of good-quality valence-to-core XES spectra for such putative species represents a technical challenge.

4. CONCLUSIONS

Diiron phthalocyanine complexes $(FePc)_2X$ (Pc = unsubstituted phthalocyanine) containing an Fe−X−Fe (X = C, N, O) core and representing a promising scaffold for the oxidation catalysis have been investigated by X-ray absorption and emission spectroscopies, as well as by theoretical calculations. The structures of three complexes, **1** (μ-carbido), **2** (μ-nitrido), and **3** (μ-oxo), have been determined by combined DFT and EXAFS studies for the first time. X-ray structures of these complexes were not yet resolved because of the low solubility of the unsubstituted phthalocyanine complexes making difficult the growth of single crystals. Their electronic structures were studied experimentally using core hole X-ray spectroscopies and simulated by DFT. The results are in agreement with the presence of Fe(IV)Fe(IV) in **1**, mixed Fe(III)−Fe(IV) in **2**, and Fe(III)Fe(III) sites in **3**. According to both DFT and EXAFS data, the Fe−X distance changes in the sequence Fe−O > Fe−C > Fe−N, suggesting the redox non-innocence of the bridging carbon in **1**.

A remarkably good correlation between the simulated Fe K pre-edge features of the complexes **1**−**3** and the experimental XANES spectra has been found. These experimental and theoretical results provide a deep insight into electronic structure and orbital mixing for the Fe−X−Fe core (X = C, N, O). The particular features of μ-nitrido dimer **2** are the highest Fe−X bond order, whereas μ-carbido dimer **1**, formally a closed-shell structure with double bonds Fe═C, has lower covalency of bridging Fe−C bond. In the sequence **1**−**3**, the most electron-rich μ-bridging oxygen of **3** forms only a single Fe−O bond, whereas the carbon bridge of **1** has too high energy of p-electrons and back-donates them to iron site. The nitrogen bridge of **2** has therefore the highest Fe−X bond covalency.

Successful DFT simulation of the properties of **1**−**3** allowed us to extend the same calculation approach on the hypothetical high-valent dirion oxo complexes **1-O**−**3-O**, bearing a terminal Fe═O bond on one of two iron atoms. The properties of the oxo species **1-O**, **2-O**, and **3-O** with μ-carbido, μ-nitrido, and μ-oxo bridges as well as their core hole spectra have been calculated by DFT.

In the oxo complexes **1-O**−**3-O**, the XANES pre-edges should be dominated by the contribution of the less symmetric iron atom not bearing a terminal oxygen. For this reason, the XAS spectra of putative oxo complexes should resemble the spectral signatures of Fe(IV) in the corresponding Fe(IV)Fe(IV) species (having no terminal Fe═O moiety), which might explain our persistent failures to observe them experimentally.

The obtained results also provide a simple tentative rationale for the exceptional activity of **2-O**, based on the stronger trans-effect of the nitrido ligand, which weakens the Fe−O terminal bond. The μ-carbido complex **1** has lower covalency of the Fe−C bridging bond, and its oxo complex **1-O** is expected to have a less reactive Fe═O terminal bond than **2-O**. However, it would be highly instructive to obtain more information on the yet unstudied catalytic properties of **1**, to check these conclusions.

■ ASSOCIATED CONTENT

Supporting Information

Additional EPR, XAS, and XES spectra; tables of DFT-calculated properties; isosurfaces of frontier molecular orbitals; *xyz* files of optimized molecular geometry; and input file headers for DFT calculations. This material is available free of charge via the Internet at http://pubs.acs.org.

■ AUTHOR INFORMATION

Corresponding Authors

*A.B.S.: e-mail, alexander.sorokin@ircelyon.univ-lyon1.fr.

*P.A.: e-mail, pavel.afanasiev@ircelyon.univ-lyon1.fr; tel, +33 472 445 466; fax, +33 472 534 499.

Notes

The authors declare no competing financial interest.

■ ACKNOWLEDGMENTS

Research support was provided by the Agence Nationale de Recherche (ANR, France, grant ANR-08-BLANC-0183-01) and by CNRS (project PICS no. 6295). C.C. is grateful to the Région Rhône-Alpes for a Ph.D. fellowship. We acknowledge the SOLEIL (Gif-sur-Yvette, France) and the European Synchrotron Radiation Facility (Grenoble, France) for provision of SAMBA and ID26 beamline, respectively.

■ REFERENCES

(1) (a) Shilov, A. E.; Shul'pin, G. B. *Chem. Rev.* **1997**, *97*, 2879−2932. (b) Copéret, C. *Chem. Rev.* **2010**, *110*, 656−680. (c) Bordeaux, M.; Galarneau, A.; Drone, J. *Angew. Chem., Int. Ed.* **2012**, *51*, 10712−10723.

(2) (a) Periana, R. A.; Taube, D. J.; Gamble, S.; Taube, H.; Satoh, T.; Fujii, H. *Science* **1998**, *280*, 560−565. (b) Kirillova, M. V.; Kuznetsov, M. L.; Reis, P. M.; da Silva, J. A. L.; Frausto da Silva, J. J. R.; Pombeiro,

A. J. L. *J. Am. Chem. Soc.* **2007**, *129*, 10531−10545. (c) Palkovits, R.; Antonietti, M.; Kuhn, P.; Thomas, A.; Schüth, F. *Angew. Chem., Int. Ed.* **2009**, *48*, 6909−6912. (d) Hammond, C.; Jenkins, R. L.; Dimitratos, N.; Lopez-Sanchez, J. A.; ab Rahim, M. H.; Forde, M. M.; Thetford, A.; Murphy, D. M.; Hagen, H.; Stangland, E. E.; Moulijn, J. M.; Taylor, S. H.; Willock, D. J.; Hutchings, G. J. *Chem.—Eur. J.* **2012**, *18*, 15735−15745. (e) Hammond, C.; Dimitratos, N.; Lopez-Sanchez, J. A.; Jenkins, R. L.; Whiting, G.; Kondrat, S. A.; ab Rahim, M. H.; Forde, M. M.; Thetford, A.; Hagen, H.; Stangland, E. E.; Moulijn, J. M.; Taylor, S. H.; Willock, D. J.; Hutchings, G. J. *ACS Catal.* **2013**, *3*, 1835−1844.

(3) Gunay, A.; Theopold, K. H. *Chem. Rev.* **2010**, *110*, 1060−1081.

(4) (a) Costas, M. *Coord. Chem. Rev.* **2011**, *255*, 2912−2932. (b) Che, C.-M.; Kar-Yan Lo, V.; Zhou, C. Y.; Huang, J.-S. *Chem. Soc. Rev.* **2011**, *40*, 1950−1975. (c) Nam, W. *Acc. Chem. Res.* **2007**, *40*, 522−531. (d) de Visser, S. P. *J. Am. Chem. Soc.* **2006**, *128*, 9813−9824. (e) Nam, W.; Lee, Y.-M.; Fukuzumi, S. *Acc. Chem. Res.* **2014**, *47*, 1146−1154. (f) de Visser, S. P.; Rohde, J.-U.; Lee, Y.-M.; Cho, J.; Nam, W. *Coord. Chem. Rev.* **2013**, *257*, 381−393.

(5) Sorokin, A. B.; Kudrik, E. V.; Bouchu, D. *Chem. Commun.* **2008**, 2562−2564.

(6) Kudrik, E. V.; Afanasiev, P.; Alvarez, L. X.; Dubourdeaux, P.; Clémancey, M.; Latour, J.-M.; Blondin, G.; Bouchu, D.; Albrieux, F.; Nefedov, S. E.; Sorokin, A. B. *Nat. Chem.* **2012**, *4*, 1024−1029.

(7) Floris, B.; Donzello, M. P.; Ercolani, C. Single-Atom Bridged Dinuclear Metal Complexes with Emphasis on Phthalocyanine System. In *The Porphyrin Handbook*; Kadish, K. M., Smith, K. M., Guilard, R., Eds.; Academic Press: Amsterdam, 2003; Vol. *18*, p 1.

(8) (a) Ercolani, C.; Gardini, M.; Pennesi, G.; Rossi, G.; Russo, U. *Inorg. Chem.* **1988**, *27*, 422−424. (b) Bottomley, L. A.; Gorce, J.-N.; Goedken, V. L.; Ercolani, C. *Inorg. Chem.* **1985**, *24*, 3733−3737.

(9) Sorokin, A. B.; Kudrik, E. V.; Alvarez, L. X.; Afanasiev, P.; Millet, J. M. M.; Bouchu, D. *Catal. Today* **2010**, *157*, 149−154.

(10) Kudrik, E. V.; Afanasiev, P.; Bouchu, D.; Millet, J. M. M.; Sorokin, A. B. *J. Porphyrins Phthalocyanines* **2008**, *12*, 1078−1089.

(11) Kudrik, E. V.; Sorokin, A. B. *Chem.—Eur. J.* **2008**, *14*, 7123−7126.

(12) Colomban, C.; P; Kudrik, E. V.; Afanasiev, P.; Sorokin, A. B. *J. Am. Chem. Soc.* **2014**, *136*, 11321−11330.

(13) Afanasiev, P.; Kudrik, E. V.; Millet, J. M. M.; Bouchu, D.; Sorokin, A. B. *Dalton Trans.* **2011**, *40*, 701−710.

(14) Afanasiev, P.; Kudrik, E. V.; ALbrieux, F.; Briois, V.; Koifman, O. I.; Sorokin, A. B. *Chem. Commun.* **2012**, *48*, 6088−6090.

(15) Murray, K. S. *Coord. Chem. Rev.* **1974**, *12*, 1−35.

(16) Ercolani, C.; Gardini, M.; Pennesi, G.; Rossi, G. *J. Mol. . Catal.* **1985**, *30*, 135−144.

(17) Silaghi-Dumitrescu, R.; Makarov, S. V.; Uta, M. M.; Dereven'kov, I. A.; Stuzhin, P. A. *New. J. Chem.* **2011**, *35*, 1140−1145.

(18) (a) Rossi, G.; Goedken, V. L.; Ercolani, C. *J. Chem. Soc. Chem. Commun.* **1988**, 46−47. (b) Ercolani, C.; Gardini, M.; Goedken, V. L.; Pennesi, G.; Rossi, G.; Russo, U.; Zanonato, P. *Inorg. Chem.* **1989**, *28*, 3097−3099.

(19) Bakshi, E. N.; Delfs, C. D.; Murray, K. S.; Peters, B.; Homborg, H. *Inorg. Chem.* **1988**, *27*, 4318−4320.

(20) Tatsumi, K.; Hoffmann, R.; Whangbo, M.-H. *J. Chem. Soc. Chem. Commun.* **1980**, 509−511.

(21) Heijboer, W. M.; Koningsberger, D. C.; Weckhuysen, B. M.; de Groot, F. M. F. *Catal. Today* **2005**, *110*, 228−238.

(22) (a) Sheng, X.; Horner, J. H.; Newcomb, M. *J. Am. Chem. Soc.* **2008**, *130*, 13310−13320. (b) Newcomb, M.; Halgrimson, J. A.; Horener, J. H.; Wasinger, E. C.; Chen, L. X.; Sligar, S. G. *Proc. Natl. Acad. Sci. U. S. A.* **2008**, *105*, 8179−8184.

(23) (a) Yosca, T. H.; Rittle, J.; Krest, C. M.; Onderko, E. L.; Silakov, A.; Calixto, J. C.; Behan, R. K.; Green, M. T. *Science* **2013**, *342*, 825−829. (b) Suchkova, S. A.; Soldatov, A.; Dziedzik-Kocurek, K.; Stillman, M. J. *J. Phys.: Conf. Ser.* **2009**, *109*, 012211.

(24) (a) Jackson, T. A.; Rohde, J.-U.; Seo, M. S.; Sastri, C. V.; DeHont, R.; Stubna, A.; Ohta, T.; Kitagawa, T.; Münck, E.; Nam, W.; Que, L., Jr. *J. Am. Chem. Soc.* **2008**, *130*, 12394−12407. (b) Chandrasekaran, P.; Stieber, S. C. E.; Collins, T. J.; Que, L., Jr.; Neese, F.; DeBeer, S. *Dalton Trans.* **2011**, *40*, 11070−11079. (c) Chanda, A.; Shan, X.; Chakrabarti, M.; Ellis, W. C.; Popescu, D. L.; de Oliveira, F. T.; Wang, D.; Que, L., Jr.; Collins, T. J.; Münck, E.; Bominaar, E. L. *Inorg. Chem.* **2008**, *47*, 3669−3678. (d) Berry, J. F.; Bill, E.; Bothe, E.; DeBeer George, S.; Mienert, B.; Neese, F.; Wieghardt, K. *Science* **2006**, *312*, 1937. (e) de Oliveira, F. T.; Chanda, A.; Banerjee, D.; Shan, X.; Mondal, S.; Que, L., Jr.; Bominaar, E. L.; Münck, E.; Collins, T. J. *Science* **2007**, *315*, 835−838.

(25) Mijovilovich, A.; Meyer-Klaucke, W. *J. Synchrotron Radiat.* **2003**, *10*, 64−68.

(26) DeBeer George, S.; Petrenko, T.; Neese, F. *J. Phys. Chem. A* **2008**, *112*, 12936−12943.

(27) Lee, N.; Petrenko, T.; Bergmann, U.; Neese, F.; DeBeer, S. *J. Am. Chem. Soc.* **2010**, *132*, 9715−9727.

(28) (a) de Visser, S. P. *J. Am. Chem. Soc.* **2010**, *132*, 1087−1097. (b) Shaik, S.; Hirao, H.; Kumar, D. *Acc. Chem. Res.* **2007**, *40*, 532−542. (c) Kumar, D.; Thiel, W.; de Visser, S. P. *J. Am. Chem. Soc.* **2011**, *133*, 3869−3980. (d) Meunier, B.; de Visser, S. P.; Shaik, S. *Chem. Rev.* **2004**, *104*, 3947−3980.

(29) Geng, C.; Ye, S.; Neese, F. *Dalton Trans.* **2014**, *43*, 6079−6086.

(30) Kudrik, E. V.; Safonova, O.; Glatzel, P.; Swarbrick, J. C.; Alvarez, L. X.; Sorokin, A. B.; Afanasiev, P. *Appl. Catal. B: Environ.* **2012**, *113*−*114*, 43−51.

(31) (a) Ercolani, C.; Gardini, M.; Monacelli, F.; Pennesi, G.; Rossi, G. *Inorg. Chem.* **1983**, *22*, 2584−2589. (b) Ercolani, C.; Gardini, M.; Murray, K. S.; Pennesi, G.; Rossi, G. *Inorg. Chem.* **1986**, *25*, 3972−3976.

(32) Stoll, S.; Schweiger, A. *J. Magn. Reson.* **2006**, *178*, 42−55.

(33) Ankudinov, A. L.; Bouldin, C. E.; Rehr, J. J.; Sims, J.; Hung, H. *Phys. Rev. B* **2002**, *65*, 104−107.

(34) Klementev, K. V. *J. Synchrotron Radiat.* **2001**, *8*, 270−272.

(35) Neese, F. *ORCA—An Ab Initio, Density Functional and Semiempirical Program Package, 2.8*, University of Bonn, Bonn, Germany, 2011; http://www.thch.uni-bonn.de/tc/orca/.

(36) Becke, A. D. *Phys. Rev. A* **1988**, *38*, 3098−3100.

(37) Weigend, A. *Phys. Chem. Chem. Phys.* **2006**, *8*, 1057−1065.

(38) Becke, A. D. *J. Chem. Phys.* **1993**, *98*, 5648−5652.

(39) Lee, C.; Yang, W.; Parr, R. G. *Phys. Rev. B* **1988**, *37*, 785−789.

(40) Hoe, W.-M.; Cohen, A. J.; Handy, N. C. *Chem. Phys. Lett.* **2001**, *341*, 319−328.

(41) Eichkorn, K.; Treutler, O.; Öhm, H.; Häser, M.; Ahlrichs, R. *Chem. Phys. Lett.* **1995**, *240*, 283−289.

(42) Neese, F.; Wennmohs, F.; Hansen, A.; Becker, U. *Chem. Phys.* **2009**, *356*, 98−109.

(43) Orio, M.; Pantazis, D. A.; Petrenko, T.; Neese, F. *Inorg. Chem.* **2009**, *48*, 7251−7260.

(44) Ruiz, E.; Rodríguez-Fortea, A.; Cano, J.; Alvarez, S.; Alemany, P. *J. Comput. Chem.* **2003**, *24*, 982−989.

(45) Yamanaka, S.; Kawakami, T.; Nagao, H.; Yamaguchi, K. *Chem. Phys. Lett.* **1994**, *231*, 25−33.

(46) Lancaster, K. M.; Roemelt, M.; Ettenhuber, P.; Hu, Y.; Ribbe, M. W.; Neese, F.; Bergmann, U.; DeBeer, S. *Science* **2011**, *334*, 974−977.

(47) Allouche, A. R. *J. Comput. Chem.* **2011**, *32*, 174−182.

(48) (a) Ercolani, C.; Floris, B. Metal phthalocyanine single-atom bridged dimers. Part 2. Recent results. In *Phthalocyanines: Properties and Applications*; Leznoff, C. C., Lever, A. B. P., Eds.; VCH: New York, 1996; Vol. *4*, p 405. (b) Ercolani, C.; Monacelli, F. *J. Porphyrins Phthalocyanines* **2001**, *5*, 668−673. (c) Ercolani, C.; Gardini, M.; Murray, K. S.; Pennesi, G.; Rossi, G.; Zwack, P. R. *Inorg. Chem.* **1987**, *26*, 3539−3543. (d) Ercolani, C.; Monacelli, F.; Dzugan, S.; Goedken, V. L.; Pennesi, G.; Rossi, G. *J. Chem. Soc., Dalton Trans.* **1991**, 1309−1315.

(49) (a) Nemykin, V. N.; Chernii, V. Ya.; Volkov, S. V.; Bundina, N. I.; Kaliya, O. L.; Li, V. D.; Luk'yanets, E. A. *J. Porphyrins Phthalocyanines* **1999**, *3*, 87−98. (b) Nemykin, V. N.; Tret'yakova, I. N.; Volkov, S. V.; Li, V. D.; Mekhryakova, N. G.; Kaliya, O. L.; Luk'yanets, E. A. *Russ. Chem. Rev.* **2000**, *69*, 325−346.

(50) Dieing, R.; Schmid, G.; Witke, E.; Feucht, C.; Dreßen, M.; Pohmer, J.; Hanack, M. *Chem. Ber.* **1995**, *128*, 589−598.
(51) Scheidt, W. R.; Summerville, D. A.; Cohen, I. A. *J. Am. Chem. Soc.* **1976**, *98*, 6623−6628.
(52) Hargittai, I. *Pure Appl. Chem.* **1989**, *61*, 651−660.
(53) Zanotti, G.; Notarantonio, S.; Paoletti, A. M.; Pennesi, G.; Rossi, G. *J. Porphyrins Phthalocyanines* **2011**, *15*, 1−8.
(54) De Groot, F. *Chem. Rev.* **2001**, *101*, 1779−1808.
(55) Glatzel, P.; Bergmann, U. *Coord. Chem. Rev.* **2005**, *249*, 65−95.
(56) Peng, G.; Degroot, F. M. F.; Hamalainen, K.; Moore, J. A.; Wang, X.; Grush, M. M.; Hastings, J. B.; Siddons, D. P.; Armstrong, W. H.; Mullins, O. C.; Cramer, S. P. *J. Am. Chem. Soc.* **1994**, *116*, 2914−2920.
(57) Tsutsumi, K.; Nakamori, H.; Ichikawa, K. *Phys. Rev. B* **1976**, *13*, 929−933.
(58) Glatzel, P.; Bergmann, U.; de Groot, F. M. F.; Cramer, S. P. *Phys. Rev. B* **2001**, *64*, 045109.
(59) Pollock, C. J.; Delgado-Jaime, M. U.; Mihail Atanasov, M.; Neese, F.; DeBeer, S. *J. Am. Chem. Soc.* **2014**, *136*, 9453−9463.
(60) Thich, J. A.; Toby, B. H.; Powers, D. A.; Potenza, J. A.; Schugar, H. J. *Inorg. Chem.* **1981**, *20*, 3314−3317.
(61) Kossmann, S.; Kirchner, B.; Neese, F. *Mol. Phys.* **2007**, *105*, 2049−2071.
(62) Conradie, M. M.; Conradie, J.; Ghosh, A. *J. Inorg. Biochem.* **2011**, *105*, 84−91.
(63) (a) Hopmann, K. H.; Conradie, J.; Ghosh, A. *J. Phys. Chem. B* **2009**, *113*, 10540−10547. (b) Thorbjørn, J.; Morsing, T. J.; Sauer, S. P. A.; Weihe, H.; Bendix, J.; Døssing, A. *Inorg. Chim. Acta* **2013**, *396*, 72−77.
(64) van Lenthe, E.; van der Avoird, A.; Wormer, P. E. S. *J. Comput. Chem.* **1998**, *108*, 4783−4796.
(65) Munzarova, M. L.; Kubacek, P.; Kaupp, M. *J. Am. Chem. Soc.* **2000**, *122*, 11900−11913.
(66) (a) Gherman, B. F.; Cramer, C. J. *Coord. Chem. Rev.* **2009**, *253*, 723−753. (b) Ciofini, I.; Daul, C. A. *Coord. Chem. Rev.* **2003**, *238*, 187−209.
(67) Bergmann, U.; Horne, C. R.; Collins, T. J.; Workman, J. M.; Cramer, S. P. *Chem. Phys. Lett.* **1999**, *302*, 119−124.
(68) (a) Delgado-Jaime, M. U.; Dible, B. R.; Chiang, K. P.; Brennessel, W. W.; Holland, P. L.; Bergmann, U.; DeBeer, S. *Inorg. Chem.* **2011**, *50*, 10709−10717. (b) Pollock, C. J.; DeBeer, S. *J. Am. Chem. Soc.* **2011**, *133*, 5594−5601.
(69) Swarbrick, J. C.; Kvashnin, Y.; Schulte, K.; Seenivasan, K.; Lamberti, C.; Glatzel, P. *Inorg. Chem.* **2010**, *49*, 8323−8332.
(70) Guemmaz, M.; Moraitis, G.; Mosser, A.; Khan, M. A.; Parlebas, J. C. *J. Alloys Compd.* **1997**, *262−263*, 397−401.
(71) Westre, T. E.; Kennepohl, P.; DeWitt, J. G.; Hedman, B.; Hodgson, K. O.; Solomon, E. I. *J. Am. Chem. Soc.* **1997**, *119*, 6297−6314.
(72) (a) Rohde, J.-U.; In, J.-H.; Lim, M. H.; Brennessel, W. W.; Bukowski, M. R.; Stubna, A.; Münck, E.; Nam, W.; Que, L., Jr. *Science* **2003**, *299*, 1037−1039. (b) Bukowski, M. R.; Koehntop, K. D.; Stubna, A.; Bominaar, E. L.; Halten, J. A.; Münck, E.; Nam, W.; Que, L., Jr. *Science* **2005**, *310*, 1000−1002. (c) Thibon, A.; England, J.; Martinho, M.; Young, V. G.; Frisch, J. R.; Guillot, R.; Girerd, J.-J.; Münck, E.; Que, L., Jr.; Banse, F. *Angew. Chem., Int. Ed.* **2008**, *47*, 7064−7067. (d) Prat, I.; Mathieson, J. S.; Güell, M.; Ribas, X.; Luis, J. M.; Cronin, L.; Costas, M. *Nat. Chem.* **2011**, *3*, 788−793. (e) Lyakin, O. Y.; Bryliakov, K. P.; Talsi, E. P. *Inorg. Chem.* **2011**, *50*, 5526−5538.
(73) (a) Groves, J. T.; Haushalter, R. C.; Nakamura, M.; Nemo, T. E.; Evans, B. J. *J. Am. Chem. Soc.* **1981**, *103*, 2884−2886. (b) Gold, A.; Jayaraj, K.; Doppelt, P.; Weiss, R.; Chottard, G.; Bill, E.; Ding, X.; Trautwein, A. X. *J. Am. Chem. Soc.* **1988**, *110*, 5756−5761. (c) Wolter, T.; Meyer-Klaucke, W.; Müther, M.; Mandon, D.; Winkler, H.; Trautwein, A. X.; Weiss, R. *J. Inorg. Biochem.* **2000**, *78*, 117−122. (d) Franke, A.; Fertinger, C.; van Eldik, R. *Angew.Chem. Int. Ed.* **2008**, *47*, 5238−5242.
(74) Rittle, J.; Green, M. T. *Science* **2010**, *330*, 933−937.
(75) (a) Takahashi, A.; Yamaki, D.; Ikemura, K.; Kurahashi, T.; Ogura, T.; Hada, M.; Fujii, H. *Inorg. Chem.* **2012**, *51*, 7296−7305. (b) Gross, Z. *J. Biol. Inorg. Chem.* **1996**, *1*, 368−371. (c) de Visser, S. P.; Tahsini, L.; Nam, W. *Chem.—Eur. J.* **2009**, *15*, 5577−5587. (d) Kang, Y.; Chen, H.; Jeong, Y. J.; Lai, W.; Bae, E. H.; Shaik, S.; Nam, W. *Chem.—Eur. J.* **2009**, *15*, 10039−10046.
(76) Sastri, C. V.; Lee, J.; Oh, K.; Lee, Y. J.; Lee, J.; Jackson, T. A.; Ray, K.; Hirao, H.; Shin, W.; Halfen, J. A.; Kim, J.; Que, L., Jr.; Shaik, S.; Nam, W. *Proc. Natl. Acad. U. S. A.* **2007**, *104*, 19181−19186.
(77) Berry, J. F.; DeBeer George, S.; Neese, F. *Phys. Chem. Chem. Phys.* **2008**, *10*, 4361−4374.
(78) Barden, C. J.; Rienstra-Kiracofe, J. C.; Schaefer, H. F. J. *Chem. Phys.* **2000**, *113*, 690−700.
(79) (a) Smith, J. M.; Subedi, D. *Dalton Trans.* **2012**, *41*, 1423−1429. (b) Berry, J. F.; Bill, E.; Bothe, E.; DeBeer George, S.; Mienert, B.; Neese, F.; Weighardt, K. *Science* **2006**, *312*, 1937−1941. (c) Scepaniak, J.; Vogel, C. S.; Khusniyarov, M. M.; Heinemann, F. W.; Meyer, K.; Smith, J. M. *Science* **2011**, *331*, 1049−1052. (d) Aliaga-Alcade, N.; DeBeer George, S.; Bill, E.; Wieghardt, K.; Neese, F. *Angew. Chem., Int. Ed.* **2005**, *44*, 2908−2912.
(80) Ye, S. F.; Neese, F. *Proc. Natl. Acad. U. S. A.* **2011**, *108*, 1228−1233.